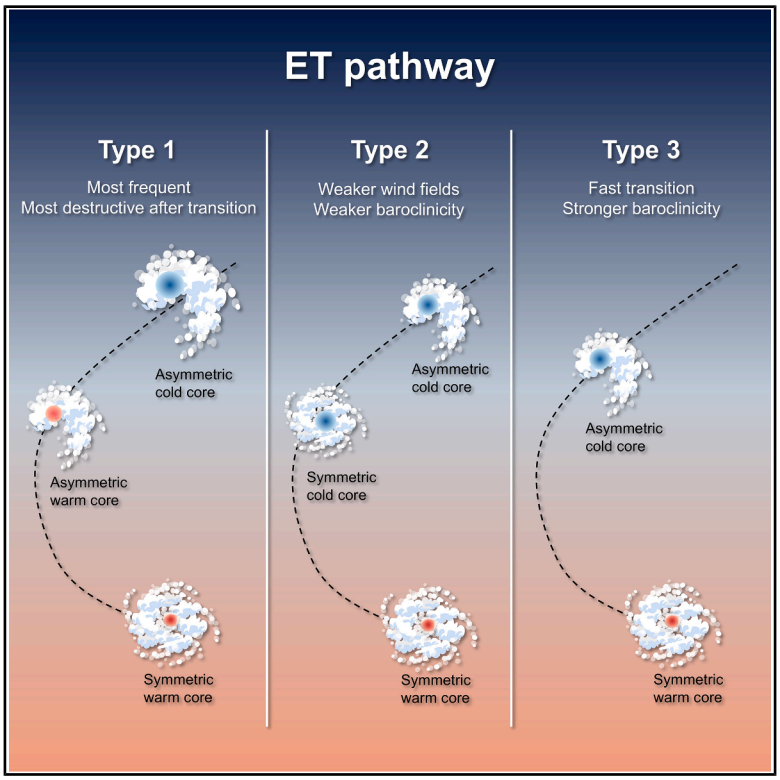
iScience

Article

Extratropical transition pathways of tropical cyclones and their associated storm intensity and destructiveness

Graphical abstract



Highlights

- Three ET pathways differ in frequency, seasonality, intensity, and environment
- Type 1 storms are the most common and the most destructive after transition
- Type 2 has weaker wind fields and transitions under weaker baroclinicity
- Type 3 meets ET criteria concurrently under strong baroclinicity

Authors

Hung Ming Cheung, Chang-Hoi Ho, Jung-Eun Chu

Correspondence

stevenhm.cheung@ewha.ac.kr (H.M.C.), hoch@ewha.ac.kr (C.-H.H.)

In brief

Earth sciences; Atmospheric science; Climatology

Cheung et al., 2025, iScience *28*, 112814
July 18, 2025 © 2025 The Author(s). Published by Elsevier Inc.
https://doi.org/10.1016/j.isci.2025.112814

CellPress

iScience

CellPress
OPEN ACCESS

Article

Extratropical transition pathways of tropical cyclones and their associated storm intensity and destructiveness

Hung Ming Cheung,[1,3,*] Chang-Hoi Ho,[1,*] and Jung-Eun Chu[2]
[1]Department of Climate and Energy Engineering, Ewha Womans University, Seoul, Republic of Korea
[2]School of Energy and Environment, City University of Hong Kong, Kowloon, Hong Kong, China
[3]Lead contact
*Correspondence: stevenhm.cheung@ewha.ac.kr (H.M.C.), hoch@ewha.ac.kr (C.-H.H.)
https://doi.org/10.1016/j.isci.2025.112814

SUMMARY

Tropical cyclones (TCs) undergoing extratropical transition (ET) can have widespread impacts; however, the differences in their evolutionary pathways remain incompletely understood. In this study, the cyclone phase space is applied to classify TCs in the western North Pacific from 1979 to 2022 into three distinct types. Type 1 exhibits the most pronounced asymmetry changes and retains the strongest surface winds, whereas Type 2 undergoes more modest asymmetry changes and maintains a weaker wind field. Type 3, in contrast, preserves a relatively symmetric wind field throughout the transition and occurs in a more baroclinic environment. Among the pathways, Type 1 demonstrates the highest post-transition destructiveness. Sensitivity analysis indicates that while most findings are robust across classification thresholds, Type 3 is particularly sensitive to threshold selection and requires careful interpretation. The present results enhance our understanding of ET variability and its implications for mid-latitude storm impacts.

INTRODUCTION

Tropical cyclones (TCs) are intense weather systems that form over warm tropical oceans, characterized by strong winds and heavy rainfall. As they move into mid-latitude regions, they encounter environmental conditions different from those in the tropics, including drier air, increased vertical wind shear, lower sea surface temperatures (SSTs), steeper SSTs, moisture, and horizontal air temperature gradients.[1–4] These changes can trigger a critical process known as the extratropical transition (ET), which significantly alters the structure and intensity of TCs.[5–7] During the ET, TCs can transform into extratropical cyclones (ETCs), which often exhibit faster movement and broader wind fields compared to their tropical counterparts.[1,8] In the western North Pacific (WNP), a highly active basin for TC activity, 27–65% of TCs experience ET.[5,9–11] This high frequency of ET events underscores the significant potential risks associated with transitioning TCs. For example, typhoon Hagibis (2019), which underwent ET before making landfall in Japan, resulted in over 90 deaths, 465 injuries, and extensive damage, including nearly 80,000 flooded or damaged homes.[12] Similarly, in the assessment of TC risks in the Republic of Korea, Nam et al.[13] highlighted the significant damage potential of weaker landfalling TCs that undergo ET.

A widely used framework for analyzing ET is the cyclone phase space (CPS; Figure 1), which provides a quantitative method for tracking the structural evolution of a TC as it transitions into an extratropical system.[14] The CPS characterizes key storm properties, including symmetry and thermal structure, through three parameters derived solely from the geopotential height: the lower-tropospheric thermal asymmetry (B), which increases with increasing asymmetry; and the thermal wind at both the lower ($-V^L_T$) and upper levels ($-V^U_T$), which distinguishes warm-core TCs ($-V^L_T \geq 0$) from cold-core ETCs ($-V^L_T < 0$). In the CPS framework, a TC typically begins as a symmetric warm-core system ($B < B_0$ and $-V^L_T \geq 0$, where B_0 is a predefined threshold) before undergoing ET. During the transition, it becomes more asymmetric and may develop a cold-core structure ($B \geq B_0$ and $-V^L_T < 0$), marking its transformation into an ETC. The CPS has gained popularity due to its ability to objectively classify storm evolution using only geopotential height data, making it a simple yet effective tool for studying ET with gridded datasets.[9,10,15–18]

In the CPS framework, the canonical ET pathway is characterized by a TC first acquiring asymmetric structure before transitioning into a cold-core ETC (referred to as Type 1 in this study). This process is reflected by an increase in the B parameter beyond B_0, followed by a shift of $-V^L_T$ from positive to negative values. However, not all TCs follow this trajectory. Some storms first develop a cold-core structure in the lower troposphere, as indicated by an early decrease in $-V^L_T$ below zero, while remaining relatively symmetric before acquiring significant asymmetry later in the transition (Type 2). A third pathway involves storms simultaneously meeting the asymmetry and cold-core structure criteria (Type 3). The classification of these ET pathways follows the conventions established in Studholme et al.[11] and Zarzycki et al.[18]

This is an open access article under the CC BY-NC license (http://creativecommons.org/licenses/by-nc/4.0/).

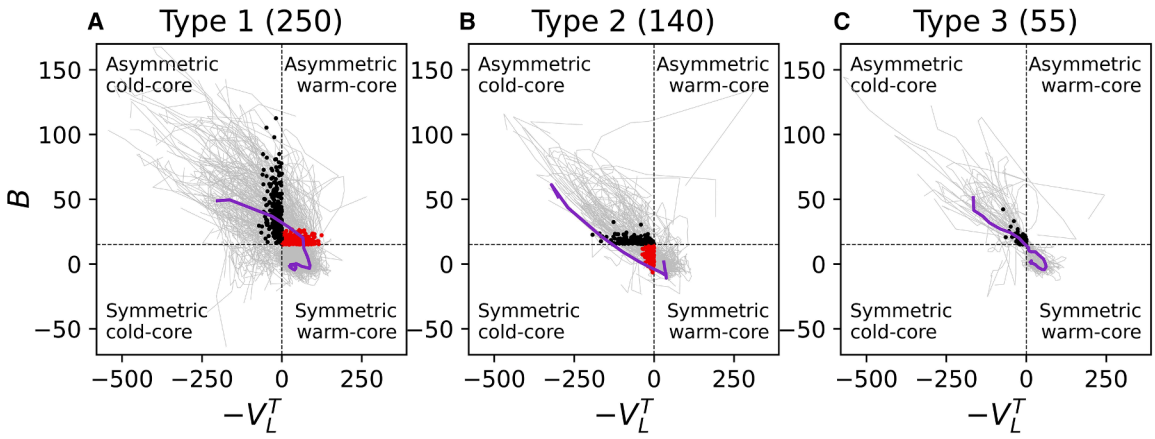


Figure 1. Cyclone phase space for the three extratropical transition pathways

The three pathways are (A) Type 1, (B) Type 2, and (C) Type 3. Each gray line represents the evolution of B and $-V^L{}_T$ throughout the lifetime of a tropical cyclone. Red and black circles indicate the onset and completion of extratropical transition, respectively. Vertical and horizontal dashed lines mark the threshold of $-V^L{}_T$ and B, respectively. The purple line demonstrates the cyclone phase space trajectory of an illustrative case from each pathway, namely (A) Nanmadol (2022), (B) Haitang, (2022), (C) Dolphin (2008). The numbers in parentheses indicates the sample size for each pathway.

Despite the significance of ET and the diversity in its structural evolution, most studies have traditionally treated ET as a unified process, without distinguishing between different transition pathways. Only a few studies have systematically classified them using CPS with reanalysis data, and these efforts have focused on relative proportion of each type or region. For example, Bieli et al.[9] quantified the proportion of each ET pathway in the WNP and other basins; Studholme et al.[11] examined global ET proportion and CPS trajectories; and Zarzycki et al.[18] analyzed ET proportion, duration, and intensity changes in the North Atlantic. A comprehensive investigation of the differences in storm transition characteristics and environmental influences among these pathways in the WNP remains limited. This study addresses TCs undergoing ET in the WNP, examining the variations in storm intensity, structure, and destructiveness among different ET pathways. Using best track and reanalysis datasets for the period 1979–2022, we classify ET cases into three distinct pathways (Types 1–3) based on CPS parameters. Through this classification, key differences in their properties and potential hazards are identified. These findings will enhance our understanding of ET variability and its implications for post-transition storm behavior.

RESULTS

Characteristics of ET pathways

To classify the ET pathways, the evolution of TCs within the CPS is analyzed using the Japanese 55-year Reanalysis (JRA-55) data. In this study, ET onset is defined as the point when a TC first exhibits an increase in asymmetry (B exceeds the threshold of 15) or acquires a cold-core structure ($-V^L{}_T < 0$). ET completion is marked by the first moment when both conditions are met. To ensure the reliability of our ET case identifications, only the 445 TCs for which ET completion is confirmed by both best track data and CPS analysis are examined. Based on this definition, the ETs in our dataset are categorized into three distinct pathways, as described in the introduction. Further details of the CPS analysis are provided in the STAR Methods section.

Types 1, 2, and 3 account for 250 (56%), 140 (32%), and 55 (12%) of the TCs, respectively. A comparison of the proportions of the three ET pathways in the WNP from previous studies[9,10] is provided in Table S1. Across these studies, Type 1 emerges as the dominant transition pathway, comprising between 59% and 71% of all ETs. Type 2 exhibits greater variability across studies, ranging from 15% to 30%, while Type 3, the least frequent and most consistent, accounts for 11–17% of cases. Findings from Wood and Ritchie[19] further support Type 1 as the predominant ET pathway in the WNP. Overall, the present classifications are consistent with previous studies.

The CPS trajectories for the three pathways are shown separately in Figure 1. Although a TC undergoing ET via any pathway requires reduced symmetry before completing the transition, the extent of symmetry change varies by pathway. Comparing the range of B during ET (from onset to completion), Type 1 shows a larger average change in B than Type 2, as indicated by the spread in black and red circles in Figures 1A and 1B, respectively. This suggests that during ET, storms following Type 1 develop greater asymmetry compared to those undergoing Type 2, while differences in the rate of change in $-V^L{}_T$ are less pronounced. For Type 3, both B and $-V^L{}_T$ remain close to their respective thresholds at the time of ET completion (Figure 1C), indicating that these storms do not exhibit strong extratropical characteristics at this stage.

Figure 2 illustrates the annual cycle of ET proportions for each ET pathway. The monthly values are determined by the timing of ET onset for Types 1 and 2, and ET completion for Type 3. Type 1 peaks in September, with the majority (76%) of events occurring between August and October. Type 2 reaches its peak slightly earlier in August but is more evenly distributed across the other months from May to November compared to Type 1. Apart from August (29%) and September (18%), five other months each contribute approximately 8–12% of the Type 2 events. Type 3

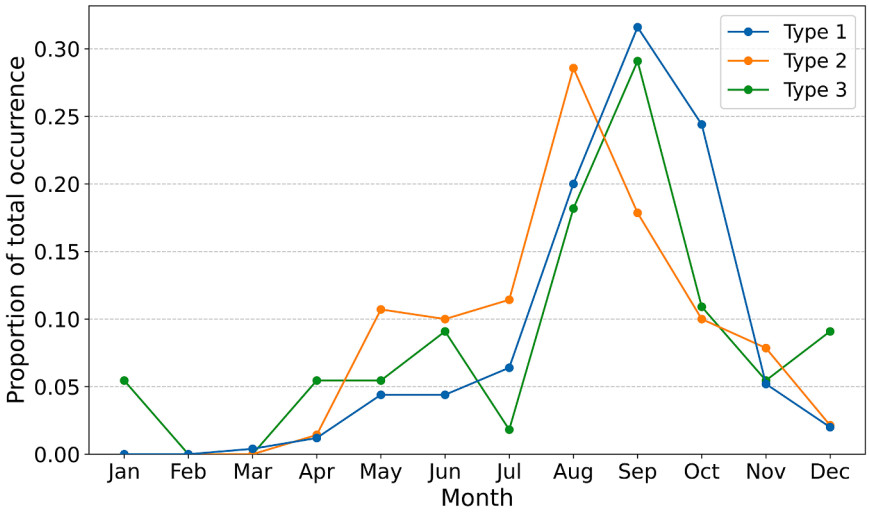


Figure 2. Annual cycle of the extratropical transition proportion for each transition pathway

primarily occurs from August to October with a maximum in September, alongside secondary peaks in June and December. Therefore, Types 1 and 3 are pronounced in late summer, while Type 2 is more prominent in early summer. A similar annual cycle was reported by Kitabatake,[10] where Types 1 and 3 were grouped together.

Next, the geographical distribution of ET onset and completion is examined in terms of latitude and longitude. At ET onset, the latitude distributions of Types 1 and 2 are similar ($p = 0.27$), but Type 2 exhibits a wider spread (Figure 3A), with its southernmost occurrence nearly 10° lower than that of Type 1. The onset longitude distributions of Types 1 and 2 are also not significantly different ($p = 0.58$), although the interquartile range for Type 1 is slightly narrower, and the two distributions largely overlap (Figure 3B). At ET completion, the mean latitude of Type 1 is higher than Types 2 and 3 (Figure 3C). A statistically significant difference in distribution among the three pathways is observed ($p = 0.0001$), primarily due to differences between Types 1 and 2 (adjusted $p = 0.01$), and between Types 1 and 3 (adjusted $p = 0.0003$) (Table S2). However, the longitude distributions at ET completion show no significant difference ($p = 0.38$) (Figure 3D). The higher completion latitude of Type 1 may be linked to its prolonged maintenance of a warm-core structure, which enhances its resistance to the erosion of tropical characteristics. Overall, aside from completion latitude, no systematic geographical difference among the three ET pathways is detected.

Storm intensity and large-scale environmental conditions

Figure 4 presents the composite 10-m wind speed at ET onset and completion, rotated to align with the direction of storm motion. In all ET pathways, the right-hand side of the storm exhibits stronger wind than the left-hand side, consistent with the composite wind patterns of storms over the WNP reported by Kitabatake.[10] Similarly, Kim et al.[20] also observed this wind field asymmetry in WNP TCs making landfall over South Korea. Within a 4-degree radius of the storm center, Type 1 exhibits the strongest surface winds at both ET onset and completion (Figures 4A and 4C). Notably, its maximum wind speed weakens from onset to completion. In contrast, Type 2 has lower maximum wind speed than Type 1 at both ET onset and completion, with no weakening observed (Figures 4B and 4D). The overall wind pattern remains largely unchanged from onset to completion for both Types 1 and 2. For Type 3 at ET completion (Figure 4E), the maximum wind speed is lower than in Type 1 but higher than in Type 2. Moreover, the contrast between the left- and right-hand side of the wind field is less pronounced in Type 3, suggesting better preservation of symmetry in the wind field. In general, significant differences in wind speed between ET pathways are observed at the 99% confidence level within a 6- to 8-degree radius of the storm center. These results are in agreement with those of Kitabatake,[10] which indicate that TCs completing ET via Types 1 and 3 tend to have lower central pressures compared to Type 2.

The dynamic and thermodynamic characteristics of the large-scale environment surrounding the storms at the time of ET completion are investigated. Figures 5A–5C presents composites of 500-hPa geopotential height, 850-hPa air temperature, and 250-hPa zonal wind within a 50° × 50° region centered on the storms. The 500-hPa height field illustrates the mid-tropospheric flow pattern and associated synoptic features (e.g., troughs and ridges) that influence storm evolution during ET completion. The 250-hPa zonal wind demonstrates the position of the upper-level jet streak, while the 850-hPa temperature distribution displays the thermal structure of the environment, with particular reference to the baroclinic zones interacting with the transitioning storm. For all pathways, the composite storm center is positioned between a trough to the west and a ridge to the east. The 5880-gpm (geopotential meter) contour, which typically indicates the subtropical high over the WNP, lies to the southeast of the storm. The 500-hPa geopotential height patterns also largely resemble those reported by Bower et al.[21] The upper-level jet stream, indicated by wind speeds $\geq$30 m s^{-1}, is located to the northeast of the storm, with its axis about 10° away from the storm center. This also indicates that the storms are approximately positioned below the right entrance region of the jet streak. Figures 5D–5F shows the meridional gradient of 500-hPa geopotential height and 850-hPa air temperature, which are key indicators of baroclinicity and help assess the strength of the large-scale forcing that influences storm evolution during ET. The temperature gradient to the north of the storm is strong, while the temperature distribution to the south is more uniform. Similarly, the geopotential height gradient is steep to the northeast of the storm but weaker to the south, except in the immediate vicinity of the storm center.

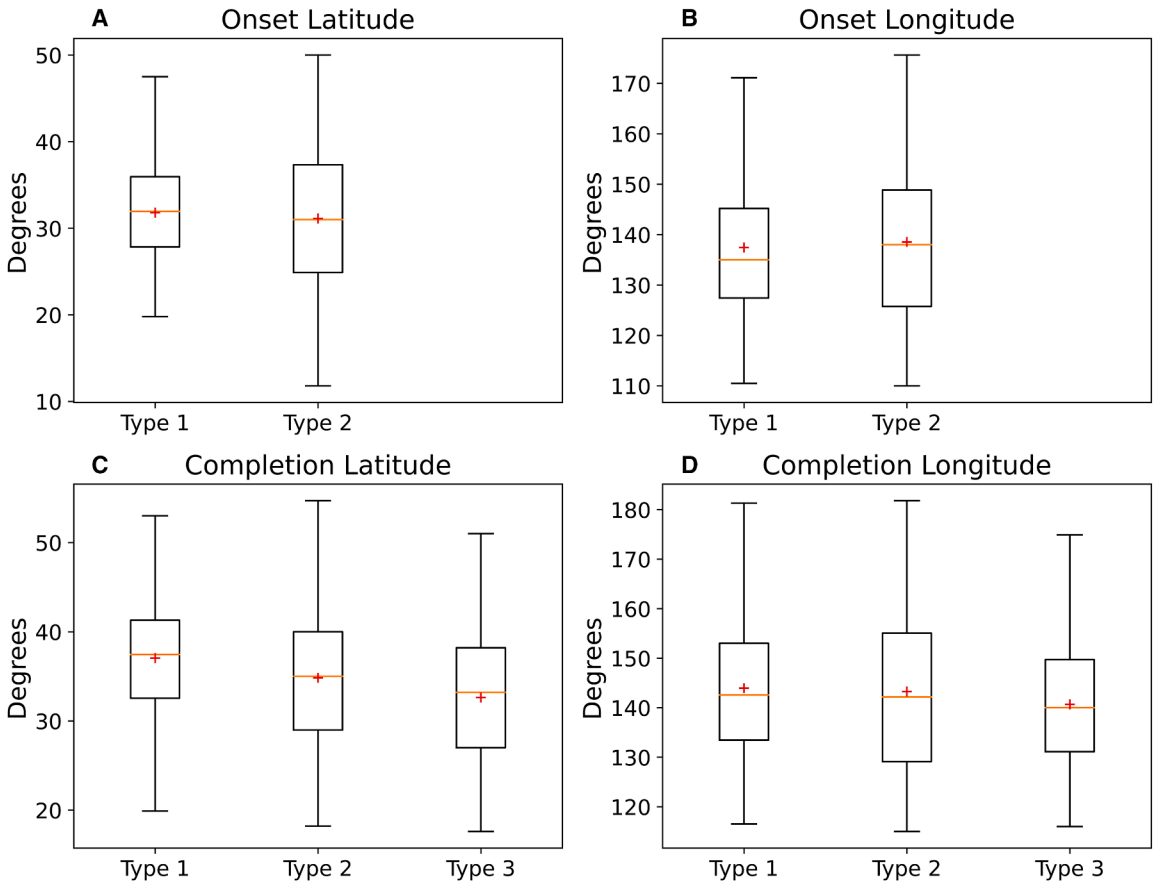


Figure 3. Geographical distribution of extratropical transition onset and completion

Boxplots depict (A) onset latitude, (B) onset longitude, (C) completion latitude, and (D) completion longitude for each extratropical transition pathway. Orange horizontal line and red plus symbol represent the median and mean, respectively. Outliers are omitted for clarity. The interquartile range is represented by box height. Note that Type 3 is excluded from (A) and (B) because its onset of extratropical transition is not defined.

Distinct differences in environmental conditions are observed among the three ET pathways. In Type 1, there is evidence of interaction with the trough as indicated by the presence of an open wave structure consistent with previous studies,[5,6] which is absent in Types 2 and 3 (Figures 5A–5C). Type 1 storms are embedded in a stronger geopotential height gradient (Figure 5D), Type 3 storms are positioned closer to the 5880-gpm contour (Figure 5C) and exhibit more pronounced geopotential height and temperature gradients over a larger area north of the storm center (Figure 5F). Although the jet streak axis remains at a similar distance from the storm center in all three types, the jet streak is weaker in Type 2 (Figure 5B). This may lead to reduced upper-level divergence and consequently weaker low-level convergence.

Overall, Type 1 storms experience a stronger baroclinic environment than Type 2, with indications of interaction with a pre-existing wave. Type 3 is associated with the strongest baroclinic environment, as reflected by the pronounced meridional gradients of geopotential height and temperature. This strong baroclinic forcing in Type 3 facilitates a rapid increase in asymmetry and transformation into a cold-core structure. These differences in environmental structure can be partially explained by the different latitude and season at which ET completion occurs. Type 1 completion tends to occur at higher latitudes (Figure 3C), where geopotential height and air temperature are generally lower, and their meridional gradients are stronger than at lower latitudes. Seasonal variability also plays a role. After summer, when Type 1 tends to peak (Figure 2), the midlatitude environment features lower geopotential heights and temperatures than in summer. Consequently, these spatial and temporal factors shape the different environmental fields associated with each ET pathway.

Destructiveness of post-transition TCs

During ET, storm wind fields expand,[1,8] enabling a transitioned TC to impact a larger area even as its maximum sustained wind speed decreases. To better assess the potential destructiveness of TCs undergoing ET, we employ integrated kinetic energy (IKE) which is an alternative metric of storm destructive potential.[16,22] The total IKE for each storm is calculated by summing over the time after ET completion until the end of record. Boxplots of the three ET pathways indicate that IKE values are concentrated in the lower range, with a tail extending toward higher values (Figure 6A). The median IKE is highest for Type 1 (0.54 GJ), followed by Type 3 (0.30 GJ) and Type 2 (0.16 GJ).

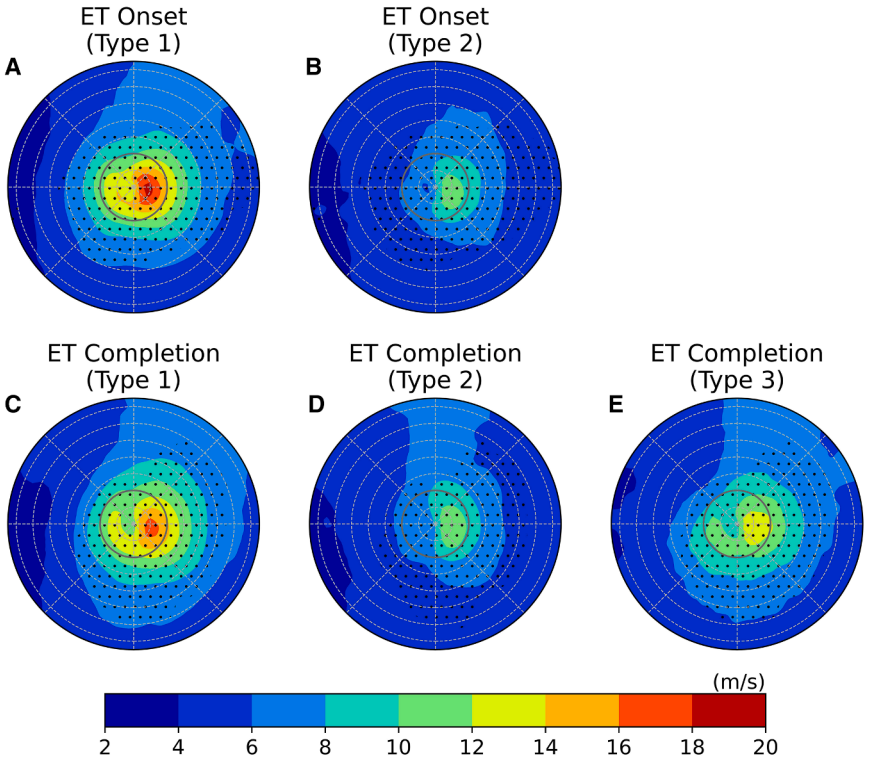


Figure 4. Storm-centered composites of 10-m wind speed at extratropical transition onset and completion

Panels show composite at (A and B) onset and (C–E) completion of extratropical transition for the three extratropical transition pathways. Each panel has a radius of 15°, with gray dashed lines marking grid intervals of 2°. A gray circle denotes a radius of 4°. Stippling indicates statistically significant differences in the median at a 99% confidence level. Before compositing, all samples are rotated so that their direction of motion aligns northward.

Type 1 also has the largest dispersion. A Kruskal-Wallis H test confirms a statistically significant difference among the three ET pathways ($p = 1.30 \times 10^{-9}$). A post-hoc test (Table S3) attributes this difference primarily to the contrast between Types 1 and 2 (adjusted $p = 5 \times 10^{-10}$), and between Types 2 and 3 (adjusted $p = 0.0073$), while the difference between Types 1 and 3 is insignificant (adjusted $p = 0.59$). It is important to note that these values, derived using a B threshold of 15, are particularly sensitive for Type 3 and should be interpreted with caution. A more detailed analysis of the effect of the B threshold on ET classification is presented in the following subsection.

Since the total IKE is influenced by the duration of the storm — longer-lasting storms tend to accumulate higher IKE— it is assessed whether the duration of the post-ET significantly affects the results. The distributions of total areas covered by wind speed $\geq$18 m s^{-1} (or high-wind area) are very similar to those of IKE (Figure 6B and Table S3). Furthermore, the post-ET storm duration does not differ significantly among the three ET pathways ($p = 0.74$), although Type 1 shows a wider dispersion (Figure 6C). Therefore, the differences in IKE among ET pathways primarily stem from variations in high-wind area rather than storm duration. However, since IKE is proportional to the square of wind speed, the greater maximum wind speed in Type 1 storms (Figure 4) likely further enhance their IKE values. Thus, the greater destructiveness associated with Type 1 may be influenced not only by broader wind fields but also by their greater wind speeds.

Sensitivity of ET classification to the threshold of *B*

When the threshold of B is lowered from 15 to 11, the distribution of ET pathways shifts with 294 (65%) cases classified as Type 1, 109 (24%) as Type 2, and 50 (11%) as Type 3. While the overall occurrence of Type 3 remains relatively stable, only 19 TCs retain their classification as Type 3 under both thresholds. The remaining Type 3 cases primarily transition to Type 1, while some Type 2 cases are reassigned to Type 3.

The analyses are reproduced for $B = 11$ (Figures S1–S5). In most cases, the adjustment of the B threshold does not lead to substantial differences. The annual cycle of ET proportions (Figures 2 and S1), geographical distribution (Figures 3 and S2), composite surface wind fields (Figures 4 and S3), and large-scale environmental conditions (Figures 5 and S4) remain largely consistent. However, there is a notable discrepancy emerges in the post-transition IKE and high-wind area for Type 3. When the threshold of B is 15, Type 3 exhibits significantly greater total IKE and high-wind area than Type 2 (Figures 6A and 6B). In contrast, when the threshold is lowered to 11, the distributions of total IKE and high-wind area for Type 3 closely resemble those of Type 2 (Figures S5A and S5B). This shift is consistent with the reclassification of cases discussed in the previous paragraph. Overall, while the main features of each ET pathway remain largely robust to changes in the B threshold, the post-transition IKE of Type 3 is particularly sensitive. Given this sensitivity, the classification of Type 3 should be interpreted with caution, as it may be subject to uncertainty depending on the B threshold chosen.

DISCUSSION

In this study, observational datasets from JRA-55 reanalysis and RSMC-Tokyo best track are analyzed in order to investigate differences in storm characteristics associated with three ET pathways in the WNP, as classified by the CPS. The findings highlight distinct features across the three pathways while also revealing the sensitivity of Type 3 to the choice of the B threshold.

The CPS analysis demonstrates that Type 1 undergoes more pronounced increases in asymmetry than Type 2, while Type 3 completes its transition abruptly and retains near-threshold properties. Temporally, Types 1 and 3 peak in September, whereas Type 2 reaches its maximum in August. Geographically,

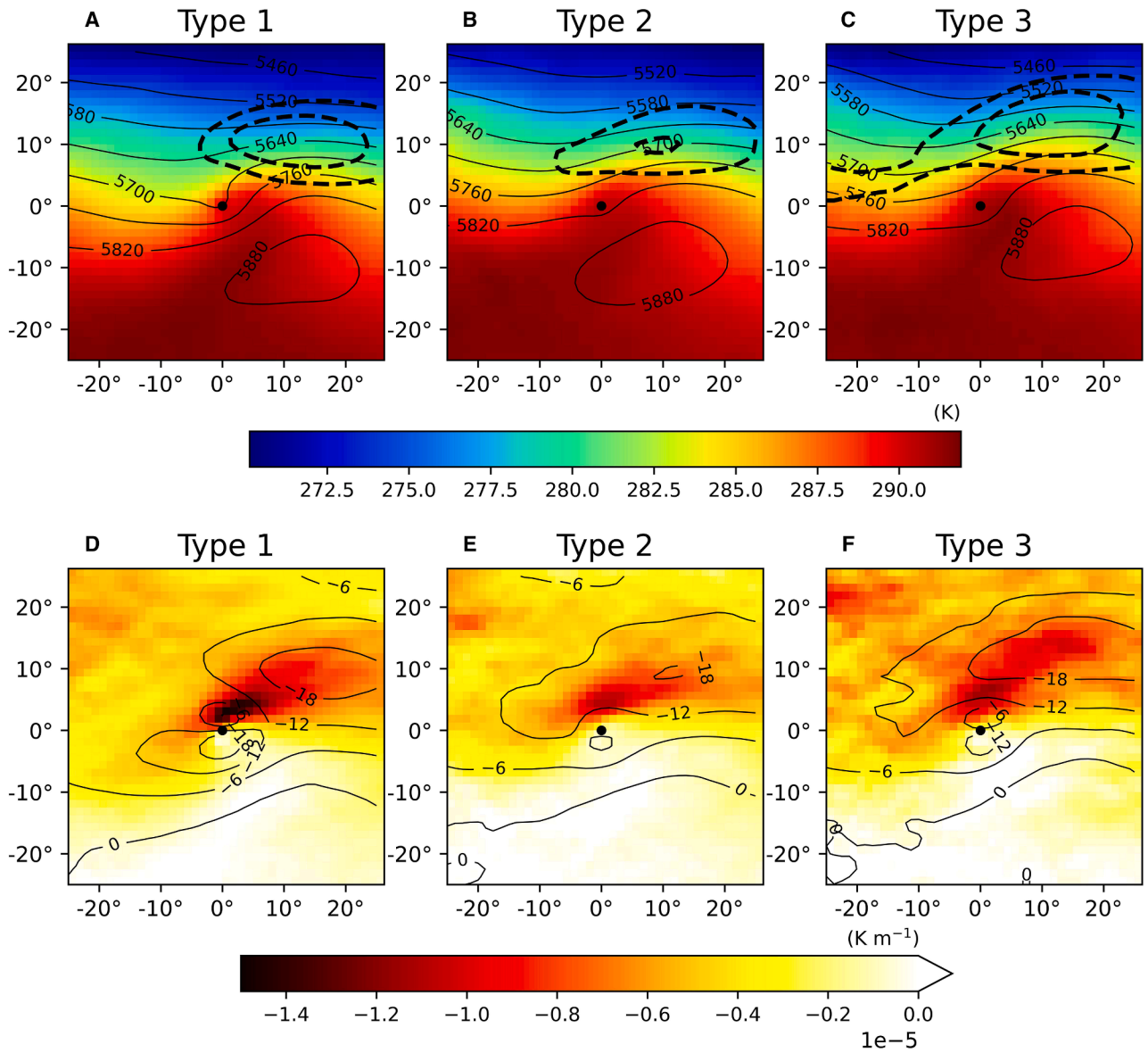


Figure 5. Large-scale environmental conditions at extratropical transition completion

(A–C) Storm-centered composite of 850-hPa air temperature (shading; K), 500-hPa geopotential height (solid contours; gpm), 250-hPa zonal wind (dashed contours; m s^{-1}), (D–F) the meridional gradient of 850-hPa air temperature (shading; K m^{-1}) and 500-hPa geopotential height (solid contours; 10^{-5} gpm m^{-1}) over a 50° × 50° domain at the completion of extratropical transition. Contours of 250-hPa zonal wind are drawn for the values exceeding 30 m s^{-1} at 10 m s^{-1} intervals. The circle at (0°, 0°) marks the location of composite storm center.

Type 1 occurs at higher latitudes at completion, with statistically significant differences in completion latitude among the three pathways. The composite surface wind field indicates that storms undergoing Type 1 ET maintain the strongest winds at ET completion. Large-scale environmental conditions at ET completion suggest that Type 3 is associated with stronger baroclinicity, characterized by steeper geopotential height and temperature gradients over a larger area to the north of storms as well as more intense upper-level jet streak. The analysis of post-transition IKE highlights that Type 1 has the highest destructive potential, followed by Types 3 and 2, indicating that Type 1 is not only the most common ET pathway but also the most destructive. However, the total IKE and high-wind area of Type 3 show notable sensitivity to the choice of B threshold, with results differing significantly when B is lowered from 15 to 11. While the overall properties of Types 1 and 2 remain largely consistent, Type 3 exhibits substantial reclassification under different thresholds, necessitating careful interpretation of its characteristics.

The distinct characteristics of the three ET pathways emphasize the significance of understanding their evolution in the context of climate change. Many studies indicate that global

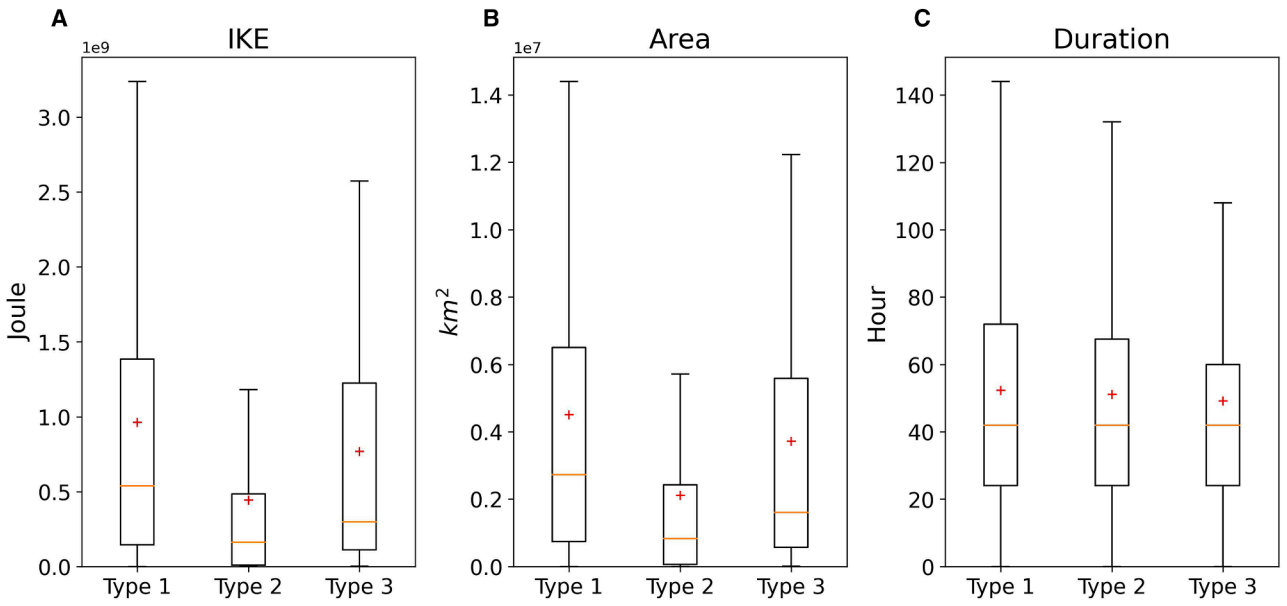


Figure 6. Integrated kinetic energy and storm characteristics after extratropical transition

Boxplots of (A) total integrated kinetic energy, (B) total area covered by winds $\geq$18 m s^{-1}, and (C) storm duration after the completion of extratropical transition. Orange horizontal line and red plus symbol represent the median and mean, respectively. Outliers are omitted for clarity. The interquartile range is represented by box height.

warming has the potential to modify ET activity in the WNP, affecting its frequency, intensity, and destructiveness.[15,16,23–25] Future research should explore how the proportions of the three ET pathways may shift under warming climate conditions and whether the observed structural differences in the current climate will endure in a changing environment.

Limitations of the study

This study classifies ET pathways based on the CPS framework; however, alternative methods exist for defining ET onset and completion. For example, Demirci et al.[26] identified the end of the transformation stage by distinguishing an open-wave structure from the geopotential height field on the 500-hPa level. Kofron et al.[27] proposed that isentropic potential vorticity could serve as a criterion for ET onset and completion, while Jung and Lackmann[28] employed surface latent heat flux and baroclinic conversion to define ET completion. Since different metrics emphasize distinct aspects of the transition process, ET pathways classification may vary depending on the chosen approach. Consequently, it remains uncertain whether the present results are directly comparable to those derived from alternative classification methods. Further research is needed to assess the robustness of the findings across different frameworks.

Another limitation of this study arises from its reliance on reanalysis data and best track data. Reanalysis data are known to systematically underestimate TC intensity (maximum sustained wind speed).[29–33] This bias primarily arises from the inherently coarse horizontal resolution of reanalysis data, which limits their ability to resolve TC features at finer scales. Capturing the fine-scale dynamics that govern TC intensification typically requires higher-resolution data.[34] However, the JRA-55 reanalysis used in this study assimilates wind profile retrievals around TCs,[35,36] which helps improve the representation of TC wind fields. As a result, the underestimation of wind speed shown in Figure 4 is likely less severe than it would be if other reanalysis data were used. Furthermore, the best track record from RSMC-Tokyo monitors TCs within a defined area of responsibility (0°–60°N, 100°E–180°). If a transitioning TC moves beyond this region, post-TC records may be incomplete and introduce uncertainty into the IKE analysis. Future studies are recommended to integrate data from multiple agencies to address this limitation.

RESOURCE AVAILABILITY

Lead contact

Further information and requests for resources should be directed to and will be fulfilled by Dr. Hung Ming Cheung (stevenhm.cheung@ewha.ac.kr).

Materials availability

This study did not generate new datasets.

Data and code availability

- This study analyzes publicly available datasets. The links are listed in the key resources table under the "Identifier" column.
- The NCL code for regridding storm wind field is publicly available and the link is listed in the key resources table under the "Identifier" column. Additional code is available upon reasonable request from the lead contact.
- Any additional information required to reanalyze the data reported in this paper is available from the lead contact upon reasonable request.

ACKNOWLEDGMENTS

This study was funded by the Korea Meteorological Administration under Grant RS-2023-00236880. J.-E.C. was supported by the Hong Kong Research Grants Council Early Career Scheme (9048309).

AUTHOR CONTRIBUTIONS

H.M.C. conceived the idea, designed the study, downloaded the data, conducted the data analysis, prepared the figures, and drafted and wrote the manuscript. C.-H.H. acquired the funding. J.-E.C. prepared the graphical abstract. H.M.C., C.-H.H., and J.-E.C. all reviewed and edited the manuscript.

DECLARATION OF INTERESTS

The authors declare no competing interests.

STAR★METHODS

Detailed methods are provided in the online version of this paper and include the following:

- KEY RESOURCES TABLE
- METHOD DETAILS
  - TC best track and reanalysis dataset
  - CPS and definition of ET pathways
  - Integrated kinetic energy
- QUANTIFICATION AND STATISTICAL ANALYSIS

SUPPLEMENTAL INFORMATION

Supplemental information can be found online at https://doi.org/10.1016/j.isci.2025.112814.

Received: March 7, 2025
Revised: April 20, 2025
Accepted: May 30, 2025
Published: June 2, 2025

REFERENCES

1. Jones, S.C., Harr, P.A., Abraham, J., Bosart, L.F., Bowyer, P.J., Evans, J. L., Hanley, D.E., Hanstrum, B.N., Hart, R.E., Lalaurette, F., et al. (2003). The extratropical transition of tropical cyclones: forecast challenges, current understanding, and future directions. Wea. Forecasting *18*, 1052–1092. https://doi.org/10.1175/1520-0434(2003)018<1052:TETOTC>2.0.CO;2.
2. Evans, C., Wood, K.M., Aberson, S.D., Archambault, H.M., Milrad, S.M., Bosart, L.F., Corbosiero, K.L., Davis, C.A., Dias Pinto, J.R., Doyle, J., et al. (2017). The extratropical transition of tropical cyclones. Part I: cyclone evolution and direct impacts. Mon. Wea. Rev. *145*, 4317–4344. https://doi.org/10.1175/MWR-D-17-0027.1.
3. Sekioka, M. (1957). A hypothesis on complex of tropical and extratropical cyclones for typhoon in the middle latitudes. J. Meteorol. Soc. Japan *35*, 170–173. https://doi.org/10.2151/jmsj1923.35.3_170.
4. Palmén, E. (1958). Vertical circulation and release of kinetic energy during the development of Hurricane Hazel into an extratropical storm. Tellus *10*, 1–13. https://doi.org/10.3402/tellusa.v10i1.9222.
5. Klein, P.M., Harr, P.A., and Elsberry, R.L. (2000). Extratropical transition of western North Pacific tropical cyclones: an overview and conceptual model of the transformation stage. Wea. Forecasting *15*, 373–395. https://doi.org/10.1175/1520-0434(2000)015<0373:ETOWNP>2.0.CO;2.
6. Harr, P.A., and Elsberry, R.L. (2000). Extratropical transition of tropical cyclones over the western North Pacific. Part I: evolution of structural characteristics during the transition process. Mon. Wea. Rev. *128*, 2613–2633. https://doi.org/10.1175/1520-0493(2000)128<2613:ETOTCO>2.0.CO;2.
7. Harr, P.A., Elsberry, R.L., and Hogan, T.F. (2000). Extratropical transition of tropical cyclones over the western North Pacific. Part II: the impact of midlatitude circulation characteristics. Mon. Wea. Rev. *128*, 2634–2653. https://doi.org/10.1175/1520-0493(2000)128<2634:ETOTCO>2.0.CO;2.
8. Evans, C., and Hart, R.E. (2008). Analysis of the wind field evolution associated with the extratropical transition of Bonnie (1998). Mon. Wea. Rev. *136*, 2047–2065. https://doi.org/10.1175/2007MWR2051.1.
9. Bieli, M., Camargo, S.J., Sobel, A.H., Evans, J.L., and Hall, T. (2019). A global climatology of extratropical transition. Part I: characteristics across basins. J. Clim. *32*, 3557–3582. https://doi.org/10.1175/JCLI-D-17-0518.1.
10. Kitabatake, N. (2011). Climatology of extratropical transition of tropical cyclones in the western North Pacific defined by using cyclone phase space. J. Meteorol. Soc. Japan *89*, 309–325. https://doi.org/10.2151/jmsj.2011-402.
11. Studholme, J., Hodges, K.I., and Brierley, C.M. (2015). Objective determination of the extratropical transition of tropical cyclones in the Northern Hemisphere. Tellus *67*, 24474. https://doi.org/10.3402/tellusa.v67.24474.
12. Moya, L., Mas, E., and Koshimura, S. (2020). Learning from the 2018 western Japan heavy rains to detect floods during the 2019 Hagibis Typhoon. Remote Sens. *12*, 2244. https://doi.org/10.3390/rs12142244.
13. Nam, C.C., Park, D.-S.R., and Ho, C.-H. (2023). Major decisive factors of tropical cyclone risk in the Republic of Korea: Intensity, track, and extratropical transition. Asia. Pac. J. Atmos. Sci. *59*, 359–366. https://doi.org/10.1007/s13143-023-00318-4.
14. Hart, R.E. (2003). A cyclone phase space derived from thermal wind and thermal asymmetry. Mon. Wea. Rev. *131*, 585–616. https://doi.org/10.1175/1520-0493(2003)131<0585:ACPSDF>2.0.CO;2.
15. Baker, A.J., Roberts, M.J., Vidale, P.L., Hodges, K.I., Seddon, J., Vannière, B., Haarsma, R.J., Schiemann, R., Kapetanakis, D., Tourigny, E., et al. (2022). Extratropical transition of tropical cyclones in a multiresolution ensemble of atmosphere-only and fully coupled global climate models. J. Clim. *35*, 5283–5306. https://doi.org/10.1175/JCLI-D-21-0801.1.
16. Cheung, H.M., and Chu, J.-E. (2023). Global increase in destructive potential of extratropical transition events in response to greenhouse warming. Npj Clim. Atmos. Sci. *6*, 137. https://doi.org/10.1038/s41612-023-00470-8.
17. Liu, M., Vecchi, G.A., Smith, J.A., and Murakami, H. (2017). The present-day simulation and twenty-first-century projection of the climatology of extratropical transition in the North Atlantic. J. Climate *30*, 2739–2756. https://doi.org/10.1175/JCLI-D-16-0352.1.
18. Zarzycki, C.M., Thatcher, D.R., and Jablonowski, C. (2017). Objective tropical cyclone extratropical transition detection in high-resolution reanalysis and climate model data. J. Adv. Model. Earth Syst. *9*, 130–148. https://doi.org/10.1002/2016MS000775.
19. Wood, K.M., and Ritchie, E.A. (2014). A 40-year climatology of extratropical transition in the eastern North Pacific. J. Clim. *27*, 5999–6015. https://doi.org/10.1175/JCLI-D-13-00645.1.
20. Kim, D., Ho, C.-H., Park, D.-S.R., and Kim, J. (2019). Influence of vertical wind shear on wind- and rainfall areas of tropical cyclones making landfall over South Korea. PLoS One *14*, e0209885. https://doi.org/10.1371/journal.pone.0209885.
21. Bower, E., Reed, K.A., Alaka, G.J., and Hazelton, A.T. (2024). Verification of operational forecast models in cases of extratropical transition of North Atlantic hurricanes. Weather Forecast. *39*, 1695–1714. https://doi.org/10.1175/WAF-D-24-0011.1.
22. Chu, J.-E., and Cheung, H.M. (2024). Extratropical Transition of Tropical Cyclones in a Changing Climate. In Advances in Hurricane Risk in a Changing Climate, J. Collins, J. Done, Y.-J. Zhu, and P. Wilson, eds. (Springer Nature Switzerland), pp. 19–41. https://doi.org/10.1007/978-3-031-63186-3_2.
23. Bieli, M., Sobel, A.H., Camargo, S.J., Murakami, H., and Vecchi, G.A. (2020). Application of the cyclone phase space to extratropical transition in a global climate model. J. Adv. Model. Earth Syst. *12*, e2019MS001878. https://doi.org/10.1029/2019MS001878.
24. Michaelis, A.C., and Lackmann, G.M. (2021). Storm-scale dynamical changes of extratropical transition events in present-day and future

high-resolution global simulations. J. Clim. *34*, 5037–5062. https://doi.org/10.1175/JCLI-D-20-0472.1.

25. Michaelis, A.C., and Lackmann, G.M. (2019). Climatological changes in the extratropical transition of tropical cyclones in high-resolution global simulations. J. Clim. *32*, 8733–8753. https://doi.org/10.1175/JCLI-D-19-0259.1.
26. Demirci, O., Tyo, J.S., and Ritchie, E.A. (2007). Spatial and spatiotemporal projection pursuit techniques to predict the extratropical transition of tropical cyclones. IEEE Trans. Geosci. Remote Sensing *45*, 418–425. https://doi.org/10.1109/TGRS.2006.882251.
27. Kofron, D.E., Ritchie, E.A., and Tyo, J.S. (2010). Determination of a consistent time for the extratropical transition of tropical cyclones. Part II: Potential vorticity metrics. Mon. Weather Rev. *138*, 4344–4361. https://doi.org/10.1175/2010MWR3181.1.
28. Jung, C., and Lackmann, G.M. (2021). The response of extratropical transition of tropical cyclones to climate change: quasi-idealized numerical experiments. J. Clim. *34*, 4361–4381. https://doi.org/10.1175/JCLI-D-20-0543.1.
29. Schenkel, B.A., and Hart, R.E. (2012). An examination of tropical cyclone position, intensity, and intensity life cycle within atmospheric reanalysis datasets. J. Clim. *25*, 3453–3475. https://doi.org/10.1175/2011JCLI4208.1.
30. Hodges, K., Cobb, A., and Vidale, P.L. (2017). How well are tropical cyclones represented in reanalysis datasets? J. Climate *30*, 5243–5264. https://doi.org/10.1175/JCLI-D-16-0557.1.
31. Aarons, Z.S., Camargo, S.J., Strong, J.D.O., and Murakami, H. (2021). Tropical cyclone characteristics in the MERRA-2 Reanalysis and AMIP simulations. Earth Space Sci. *8*, e2020EA001415. https://doi.org/10.1029/2020EA001415.
32. Murakami, H. (2014). Tropical cyclones in reanalysis data sets. Geophys. Res. Lett. *41*, 2133–2141. https://doi.org/10.1002/2014GL059519.
33. Jourdain, N.C., Barnier, B., Ferry, N., Vialard, J., Menkes, C.E., Lengaigne, M., and Parent, L. (2014). Tropical cyclones in two atmospheric (re)analyses and their response in two oceanic reanalyses. Ocean Model. (Oxf.) *73*, 108–122. https://doi.org/10.1016/j.ocemod.2013.10.007.
34. Davis, C.A. (2018). Resolving tropical cyclone intensity in models. Geophys. Res. Lett. *45*, 2082–2087. https://doi.org/10.1002/2017GL076966.
35. Kobayashi, S., Ota, Y., Harada, Y., Ebita, A., Moriya, M., Onoda, H., Onogi, K., Kamahori, H., Kobayashi, C., Endo, H., et al. (2015). The JRA-55 Reanalysis: General specifications and basic characteristics. J. Meteorol. Soc. Japan. *93*, 5–48. https://doi.org/10.2151/jmsj.2015-001.
36. Ebita, A., Kobayashi, S., Ota, Y., Moriya, M., Kumabe, R., Onogi, K., Harada, Y., Yasui, S., Miyaoka, K., Takahashi, K., et al. (2011). The Japanese 55-year Reanalysis "JRA-55": An interim report. Sola *7*, 149–152. https://doi.org/10.2151/sola.2011-038.
37. Hatsushika, H., Tsutsui, J., Fiorino, M., and Onogi, K. (2006). Impact of wind profile retrievals on the analysis of tropical cyclones in the JRA-25 Reanalysis. J. Meteorol. Soc. Japan. *84*, 891–905. https://doi.org/10.2151/jmsj.84.891.
38. Powell, M.D., and Reinhold, T.A. (2007). Tropical cyclone destructive potential by integrated kinetic energy. Bull. Am. Meteorol. Soc. *88*, 513–526. https://doi.org/10.1175/BAMS-88-4-513.
39. Kruskal, W.H., and Wallis, W.A. (1952). Use of ranks in one-criterion variance analysis. J. Am. Stat. Assoc. *47*, 583–621. https://doi.org/10.1080/01621459.1952.10483441.
40. Mann, H.B., and Whitney, D.R. (1947). On a test of whether one of two random variables is stochastically larger than the other. Ann. Math. Statist. *18*, 50–60.
41. Dunn, O.J. (1964). Multiple comparisons using rank sums. Technometrics *6*, 241–252. https://doi.org/10.1080/00401706.1964.10490181.

STAR★METHODS

KEY RESOURCES TABLE

REAGENT or RESOURCE	SOURCE	IDENTIFIER
Deposited data		
JRA-55 Reanalysis	Japan Meteorological Agency	https://doi.org/10.5065/D6HH6H41
RSMC-Tokyo best track	Japan Meteorological Agency	https://www.jma.go.jp/jma/jma-eng/jma-center/rsmc-hp-pub-eg/besttrack.html
Software and algorithms		
Regridding of storm wind field (rectilinear to polar grid)	NCL	https://www.ncl.ucar.edu/Applications/Scripts/grid2geocircle.ncl

METHOD DETAILS

TC best track and reanalysis dataset

This study analyzes the best track data from the Regional Specialized Meteorological Center (RSMC) Tokyo-Typhoon Center, spanning the period 1979–2022. This dataset provides records of TCs in the WNP, including their center location and intensity. We focus on the 539 TCs that are classified as ''extratropical cyclone'' at some point during their lifecycle. To enhance confidence in the identified ET cases, we consider only the 445 TCs for which ET completion is identified in both the best track data and through CPS analysis. While the timing of ET completion from these two sources generally agrees, minor discrepancies may occur as noted by Kitabatake.[10]

To characterize TC structure and the associated atmospheric environment, we use the Japanese 55-year Reanalysis (JRA-55) dataset, which has a horizontal grid spacing of 1.25 ° × 1.25 ° and is archived at 6-h intervals from the Japan Meteorological Agency.[35] This dataset incorporates assimilated wind profiles derived from the best track data.[36,37] From this dataset, we extract geopotential height at various pressure levels for CPS analysis, along with the following atmospheric variables: 500-hPa geopotential height, 850-hPa air temperature, 200-hPa zonal wind speed, and surface-level zonal and meridional wind speeds.

CPS and definition of ET pathways

The analysis centers on two parameters: the thermal symmetry parameter (B) and the lower-tropospheric thermal wind parameter ($-V^L_T$). The B parameter quantifies the frontal characteristics of a cyclone by measuring the storm-motion-relative thickness asymmetry between 900 and 600 hPa across the system. It is computed using the formula

$$B = h\left(\overline{Z_{600\ hPa} - Z_{900\ hPa}}|_{right} - \overline{Z_{600\ hPa} - Z_{900\ hPa}}|_{left}\right) \quad \text{(Equation 1)}$$

where Z represents the geopotential height, h is assigned to 1 and −1 when a TC is located in the Northern Hemisphere and the Southern Hemisphere, respectively, while an overbar indicates averaging within a 500-km radius on the left-/right-hand side of the TC. Meanwhile, the $-V^L_T$ parameter characterizes the vertical thermal structure (i.e., the presence of warm core or cold core) by examining the vertical gradient of the horizontal geopotential height distribution in the lower atmosphere. It is computed using the formula

$$-V^L_T = \frac{\partial(\Delta Z)}{\partial \ln p}\Big|^{600\ hPa}_{900\ hPa} \quad \text{(Equation 2)}$$

where ΔZ is the geopotential height perturbation (Z_{max} minus Z_{min}) calculated within a 500-km radius from the TC center, and p is the pressure level (either 600 or 900 hPa). A five-point running average is applied to both parameters to reduce noise. The missing values due to running average at both the beginning and end of the sequence of the two parameters are filled with the corresponding unsmoothed values.

TCs typically exhibit symmetric structure with warm cores which manifest as small B values and positive $-V^L_T$ values. In contrast, ETCs display asymmetric structure with cold cores characterized by large B values and negative $-V^L_T$ values. Following Zarzycki et al.,[18] a threshold of $B = 15$ is adopted to differentiate between symmetric and asymmetric storms. ET onset is identified when a TC either becomes asymmetric ($B > 15$) or acquires cold-core structure ($-V^L_T < 0$). By the same token, ET completion is considered as the first instance when these two conditions are satisfied. Since a TC can jump between two quadrants in the CPS multiple times during its lifetime, we define ET onset as the last time it moves from the lower-right (symmetric warm core) to the upper-right

(asymmetric warm core) or lower-left quadrant (symmetric cold core), and ET completion as the first time it moves to the upper-left quadrant (asymmetric cold core) from another quadrant. Accordingly, there are three possible ET pathways: gaining asymmetry before transforming into an ETC (Type 1); acquiring a cold-core structure first before completing transition (Type 2); and developing both asymmetric and cold-core structure at the same time step (Type 3).

Integrated kinetic energy

Following Powell and Reinhold,[38] integrated kinetic energy (IKE) at a given time step is defined as

$$IKE = \int_V \frac{1}{2}\rho U^2 dV = \frac{1}{2}\int_A U^2 dA \quad \text{(Equation 3)}$$

where ρ is the air density (=1 kg m^{-3}), U represents the surface wind speed field, V and A denote volume and area, respectively. IKE is calculated by considering only the grid points with U greater than 18 m s^{-1} within 1000-km radius from the TC center in the present study.

QUANTIFICATION AND STATISTICAL ANALYSIS

To ascertain whether differences in properties exist between the three ET pathways, we use the Kruskal-Wallis *H*-test[39] and the two-tailed Mann-Whitney *U* test,[40] which assess differences in the location of distributions. They serve as the non-parametric alternatives to one-way ANOVA and Student's *t*-test, respectively. The Mann-Whitney *U* test is applied to ET onset as this stage is not defined for Type 3 pathway. For ET completion, we first perform Kruskal-Wallis *H*-test to determine if there is a significant difference among the three pathways. If the Kruskal-Wallis *H*-test yields a significant result, we conduct post-hoc pairwise comparisons using Dunn's test,[41] which accounts for the rank-based nature of the data. To control for the familywise error rate due to multiple comparisons, the Bonferroni correction is applied, where the *p*-value for each pairwise test is multiplied by the number of comparisons, ensuring a more stringent threshold for statistical significance. The Kruskal-Wallis *H*-test and the two-tailed Mann-Whitney *U* test are performed using Scipy v1.10.1, while Dunn's test is performed using Scikit-posthocs v0.9.0. The table below provides an overview of our statistical analysis framework which includes the specific statistical tests applied to each variable, their corresponding *p*-values, and subsequent post-hoc test where applicable.

Variable	Statistical test	*p*-value	Post-hoc test
ET onset latitude	Mann-Whitney *U* test	0.27	N/A
ET onset longitude	Mann-Whitney *U* test	0.58	N/A
ET completion latitude	Kruskal-Wallis *H*-test	0.0001	Dunn's test with Bonferroni correction (Table S2)
ET completion longitude	Kruskal-Wallis *H*-test	0.38	N/A
Total IKE	Kruskal-Wallis *H*-test	1.30×10^{-9}	Dunn's test with Bonferroni correction (Table S3)
Total area	Kruskal-Wallis *H*-test	2.59×10^{-9}	Dunn's test with Bonferroni correction (Table S3)